Geometrical effects of a subducted seamount on stopping megathrust ruptures

Hongfeng Yang,[1,2] Yajing Liu,[1,3] and Jian Lin[1]

Received 6 March 2013; revised 18 April 2013; accepted 25 April 2013; published 30 May 2013.

[1] We have numerically simulated dynamic ruptures along a "slip-weakening" megathrust fault with a subducted seamount of realistic geometry, demonstrating that seamounts can act as a barrier to earthquake ruptures. Such barrier effect is calculated to be stronger for increased seamount normal stress relative to the ambient level, for larger seamount height-to-width ratio, and for shorter seamount-to-nucleation distance. As the seamount height increases from 0 to 40% of its basal width, the required increase in the effective normal stress on the seamount to stop ruptures drops by as much as ~20%. We further demonstrate that when a seamount is subducted adjacent to the earthquake nucleation zone, coseismic ruptures can be stopped even if the seamount has a lower effective normal stress than the ambient level. These results indicate that subducted seamounts may stop earthquake ruptures for a wide range of seamount normal stress conditions, including the case of the thrust fault being lubricated by seamount-top fluid-rich sediments, as suggested from observations in the Japan and Sunda Trenches. **Citation:** Yang, H., Y. Liu, and J. Lin (2013), Geometrical effects of a subducted seamount on stopping megathrust ruptures, *Geophys. Res. Lett.*, *40*, 2011–2016, doi:10.1002/grl.50509.

1. Introduction

[2] Subducted seamounts have been suggested to act as asperities where large thrust earthquakes nucleate [*Cloos*, 1992; *Husen et al*., 2002; *Hicks et al*., 2012], and as barriers to inhibit coseismic rupture propagation [*Kodaira et al*., 2000; *Mochizuki et al*., 2008]. Such barrier effect is characterized by various conceptual models. For instance, subducted seamounts have been suggested to increase normal stress on the thrust interface [*Scholz and Small*, 1997], and such seamount-induced additionally frictional resistance could stop coseismic ruptures [*Kodaira et al*., 2000]. On the other hand, subducted seamounts have also been suggested to cause erosion of overriding plate and to deliver fluid-rich sediments into seismogenic zone [*Bangs et al*., 2006]. The presence of entrained fluid-rich sediments in the vicinity of a subducted seamount would reduce effective normal stress and lubricate the thrust interface, leading to little elastic strain accumulation and thus inhibiting coseismic ruptures [*Mochizuki et al*., 2008; *Singh et al*., 2011]. Furthermore, it was proposed that seamount subduction may create a complex fracture network in the overriding plate, making it unfavorable for the generation of large earthquakes [*Wang and Bilek*, 2011]. Thus, the specific mechanisms for subducted seamounts to stop coseismic ruptures could be complex and remain open for debate.

[3] Previous numerical studies have modeled a subducted seamount as a patch under elevated effective normal stress on planar subduction fault [*Duan*, 2012; *Yang et al*., 2012], showing that the subducted seamount could slow down or stop coseismic ruptures, acting as a barrier. If such a barrier is broken, it may produce large concentrated coseismic slip as suggested for the 2011 Tohoku *Mw* 9.0 earthquake [*Simons et al*., 2011; *Duan*, 2012]. However, these planar subduction zone models have not considered the geometrical irregularities caused by a subducted seamount. Hence, its barrier effect is only realized by increasing the local effective normal stress unless other heterogeneities in friction parameters are introduced. Is it possible for a seamount to stop ruptures even with a reduction in normal stress due to the presence of fluid-rich sediments as observations in the Japan Trench and Sumatra subduction zone imply [*Bangs et al*., 2006; *Mochizuki et al*., 2008; *Singh et al*., 2011]? In this study we take into account both the geometry and local normal stress changes on a megathrust fault due to a subducted seamount [*Scholz and Small*, 1997; *Bangs et al*., 2006]. Specifically, we investigate how a seamount geometrical high under either elevated or reduced normal stress would influence coseismic rupture propagation by performing numerical simulations of dynamic ruptures using a Computational Infrastructure for Geodynamics open-source finite element tool, PyLith (http://www.geodynamics.org/cig/software/pylith) [*Aagaard et al*., 2008]. PyLith has been tested in a series of Southern California Earthquake Center dynamic rupture benchmark verifications [*Harris et al*., 2009].

2. Fault Model and Parameters

[4] We set up a 2-D subduction fault model in a homogeneous elastic half space. The subduction fault dips at θ=15° and extends 150 km in down-dip distance from the trench (Figure 1a). The domains have a shear wave velocity V_s=3.33 km/s, *P* wave velocity V_p=5.77 km/s, shear modulus μ=30 GPa, and Poisson's ratio v=0.25. These parameters are kept constant for all simulation cases. The geometry of a

Additional supporting information may be found in the online version of this article.

[1]Department of Geology and Geophysics, Woods Hole Oceanographic Institution, Woods Hole, Massachusetts, USA.
[2]School of Earth and Atmospheric Sciences, Georgia Institute of Technology, Atlanta, Georgia, USA.
[3]Department of Earth and Planetary Sciences, McGill University, Montréal, Quebec, Canada.

Corresponding author: H. Yang, School of Earth and Atmospheric Sciences, Georgia Institute of Technology, Atlanta, GA 30332, USA. (hyang@gatech.edu)

0094-8276/13/10.1002/grl.50509

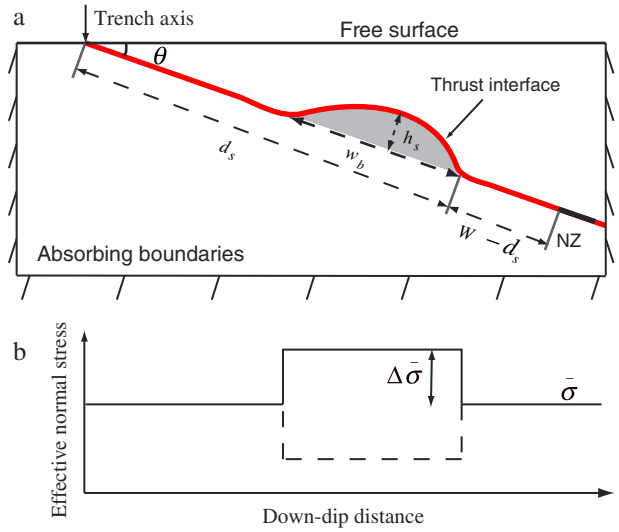

Figure 1. (a) A schematic plot of the subduction fault model and a subducted seamount (grey). Red line denotes the megathrust interface. w_b and h_s are basal width and height of the seamount (not to scale), respectively. θ is the dip angle of the subduction fault. d_s represents the distance from the trench to the down-dip edge of the seamount. W is the distance from trench to the up-dip edge of the rupture nucleation zone (NZ, black bar). (b) Schematic effective normal stress on the fault. $\Delta\bar{\sigma}$ is the perturbation in local normal stress induced by the seamount relative to the ambient level. Dashed line indicates that $\Delta\bar{\sigma}$ could be negative.

subducted seamount is characterized by two parameters, its basal width w_b and its height h_s (Figure 1a). Another important model parameter is the seamount-to-trench distance, d_s. In rate-state earthquake cycles simulations, *Yang et al.* [2012] showed that, when the total subduction fault length and the depth of earthquake nucleation are both fixed (Figure 1a), d_s determines whether ruptures will be stopped or initiate on the seamount.

[5] Here we simulate dynamic rupture scenarios using a linear slip-weakening friction law [*Ida*, 1972], in which the friction coefficient f is given by

$$f = \begin{cases} f_s - (f_s - f_d)\delta/d_0 & \delta < d_0 \\ f_d & \delta \geq d_0, \end{cases} \quad (1)$$

where δ is slip on the fault, f_s and f_d are coefficients of static and dynamic friction, and d_0 is the critical slip distance. To focus on the seamount and coseismic rupture interaction, we define the seismogenic zone to be within vertical depth of 3 to 35 km, and set an artificially large value of f_s=500 beyond the seismogenic zone to prevent further up-dip and down-dip rupture propagation. Values for friction parameters in the seismogenic zone are listed in Table 1. The normal stress on the fault σ is assumed to be $\rho_c gz$ where ρ_c is density of crust, g is gravitational acceleration, and z is depth. Pore fluid pressure in subduction zones has been proposed as overhydrostatic, even near-lithostatic at the up-dip and down-dip ends of the seismogenic zone [*Saffer and Tobin*, 2011]. Here we choose a uniform ambient effective normal stress at depth

Table 1. Stress and Friction Parameters Used in Simulations

Parameters	Values
Static friction coefficient, f_s	0.630
Dynamic friction coefficient, f_d	0.525
Effective normal stress $\bar{\sigma}$ (MPa)	50
Initial shear stress τ_0 (MPa)	28
Shear stress within nucleation zone τ_{nucl} (MPa)	31.7
Critical slip distance d_0 (m)	0.40

for simplicity (e.g., $\bar{\sigma} = 50$ MPa) [*Rice*, 1992]. In addition, the effective normal stress is assumed to be time-constant, thus does not incorporate any potential pore pressure changes induced by dilatancy or thermal pressurization during earthquakes [*Liu*, 2013; *Segall et al.*, 2010; *Noda and Lapusta*, 2010]. Coseismic ruptures are nucleated from a 3 km segment located at W = 130 km, where W is the down-dip distance between the trench axis and the up-dip edge of the nucleation zone. The initial shear stresses within the nucleation zone are prescribed slightly higher than the static strength on the fault (Table 1). The size and depth of the nucleation zone are fixed in all simulation cases; its size is just over the theoretical estimate of crack length required for instability [*Uenishi and Rice*, 2003]. After nucleation, ruptures propagate spontaneously on the fault.

[6] To adequately resolve the rupture process, grid size Δx on the fault needs to be small enough to resolve a cohesive zone. For a linear slip-weakening law in 2-D cases, *Day et al.* [2005] derived the size of the cohesive zone for a mode II rupture as

$$\Lambda_0 = \frac{9\pi}{32}\frac{\mu}{1-\nu}\frac{d_0}{\tau_s - \tau_d}, \quad (2)$$

where $\tau_s = f_s\bar{\sigma}$ and $\tau_d = f_d\bar{\sigma}$ are static and dynamic shear stresses, respectively. Using the values of parameters above and given in Table 1, we estimate Λ_0 ~2600 m, which needs to span at least 3–5 grids [*Day et al.*, 2005]. In this study, we use Δx=100 m on the fault, resulting in $\Lambda_0/\Delta x \approx 26$, a much finer resolution than the minimum requirement. Time step, Δt, needs to be smaller than the time for P wave traveling across one grid. We here use Δt=0.005 s, much less than the value of 0.017 s obtained from $\Delta x/V_p$, and thus satisfying the numerical modeling requirement.

[7] In addition to considering a seamount with realistic geometry, we assume that the seamount will change the local effective normal stress by an amount of $\Delta\bar{\sigma}$, following previous numerical approaches [*Duan*, 2012; *Yang et al.*, 2012]. According to the analysis by *Scholz and Small* [1997], the amplitude of $\Delta\bar{\sigma}$ can span a range of 0–200 MPa, depending on the material properties of the overriding plate

Table 2. Range of Geometrical Parameters for a Modeled Seamount

d_s (km)	w_b (km)	h_s (km)
60	0	0
70	10	1
80	20	2
90	30	3
100	40	4
110		
120		

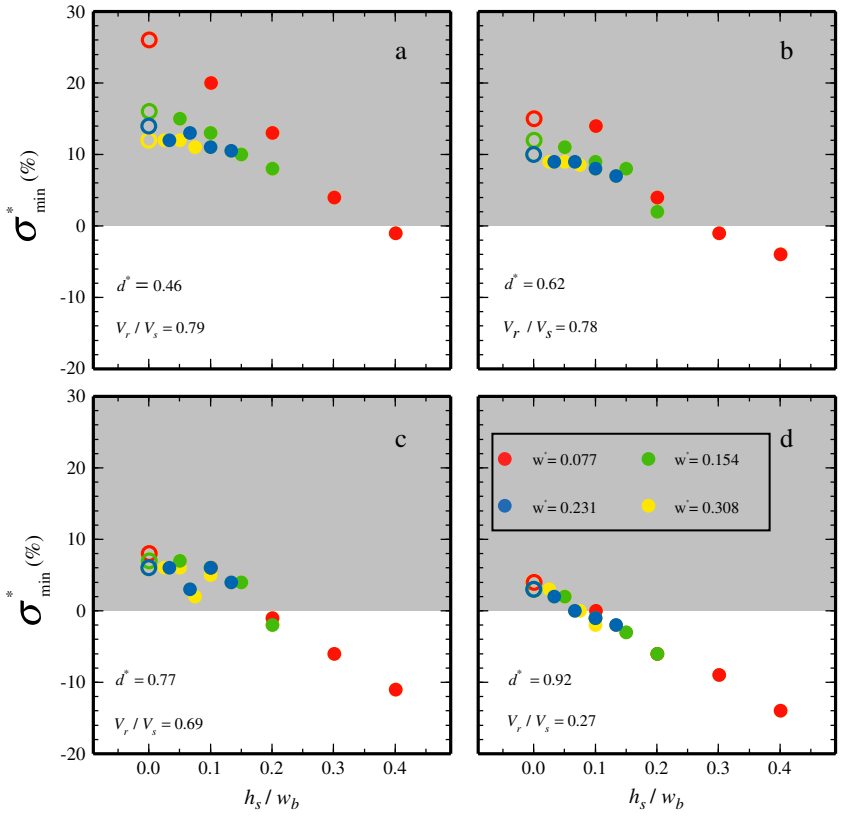

Figure 2. Effects of seamount height h_s, basal width w_b, and down-dip distance d_s on σ^*_{min}(minimum $\Delta\bar{\sigma}/\bar{\sigma}$ required to stop a rupture). (a) $d^* = 0.46$, (b) $d^* = 0.62$, (c) $d^* = 0.77$, and (d) $d^* = 0.92$. $d^* = d_s/W$ and $w^* = w_b/W$. V_r/V_s represents rupture speed normalized by the seismic shear wave velocity. Grey area denotes the regime of positive σ^*_{min}. Open circles represent the results of planar subduction fault models (i.e., $h_s = 0$). Values of the seamount basal width w_b are shown by colors.

[*Yang et al.*, 2012]. In this study, we also allow negative values of $\Delta\bar{\sigma}$, i.e., a reduction in effective normal stress on the seamount relative to the ambient normal stress on the subduction fault (Figure 1b). The sizes of seamounts that have been identified in global subduction zones range from ~10 to ~50 km in basal width and up to 4 km in height [*Kodaira et al.*, 2000; *Mochizuki et al.*, 2008; *Singh et al.*, 2011; *Trehu et al.*, 2012; *Hicks et al.*, 2012]. Therefore, we vary the values of w_b and h_s in these ranges (Table 2). To compare and apply our results to a wide range of subduction zone models, we adopt dimensionless quantities for $\sigma^* = \Delta\bar{\sigma}/\bar{\sigma}$ in percentage. Similarly, we use normalized d^* and w^* to represent the seamount-to-trench distance and basal width, respectively, where $d^* = d_s/W$ and $w^* = w_b/W$. In the current model set up where the nucleation zone size and depth are fixed, a larger d^* is equivalent to a shorter distance between the seamount and the rupture nucleation zone.

3. Results

[8] For reference, we first determine the minimum additional normal stress σ^*_{min} for a subducted seamount to stop a coseismic rupture in a planar subduction fault model, i.e., h_s=0. We run dynamic rupture simulations given a seamount size w^* and location d^* with a stress perturbation σ^*. After each simulation, we inspect the final slip distribution on the subduction fault. Because the rupture is nucleated down-dip of the seamount, the final slip up-dip of the seamount would be zero if the rupture is completely stopped by the seamount (Figure S1). Thus, we obtain the values of σ^*_{min} for every group of seamount location and basal width (Figure S2). Apparently the amplitudes of σ^*_{min} are dependent on the distance d^* and the basal width w^*. The closer the seamount is to the rupture nucleation zone (i.e., larger d^*), the smaller the σ^*_{min} would be required for the seamount to stop rupture. In the cases we simulated, the largest value of σ^*_{min}=26% is associated with a seamount of d^*=0.46 and w^*=0.077 (Figures 2a and S2). This means that the effective normal stress of the seamount patch has to be at least 26% higher than the ambient background normal stress to stop a coseismic rupture. In contrast, for a seamount with the same basal width w^*=0.077 but located at d^*=0.92, the required σ^*_{min} is only 4% (Figures 2d and S2). Furthermore, it is easier for a larger seamount to impede a rupture. For a seamount with the identical d^*, the required normal stress perturbation on the seamount σ^*_{min} to stop ruptures becomes smaller if the basal width w^* increases (Figures 2 and S2), although the difference nearly diminishes as the seamount gets very close to the nucleation zone (Figure 2d). In addition, we find that for the cases ignoring seamount heights (i.e., h_s=0), the values of σ^*_{min} are all positive, indicating $\bar{\sigma}$ on the seamount has to be higher than the ambient effective normal stress on the megathrust fault to stop ruptures.

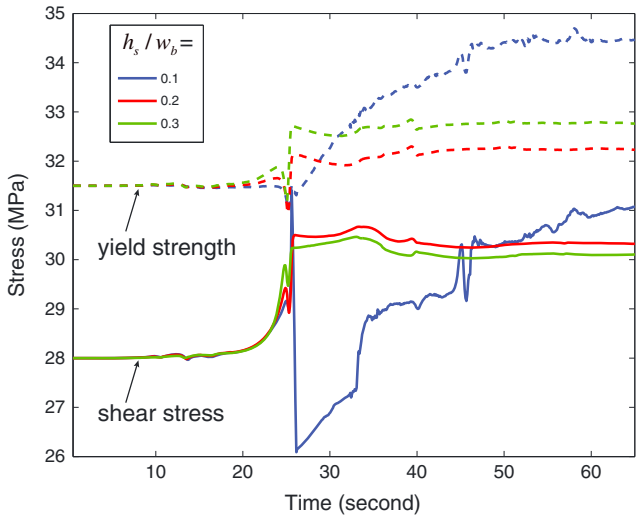

Figure 3. Stress at the top of a seamount as a function of time. The seamount has a basal width of 10 km and is located at $d^* = 0.77$. There is no stress perturbation to the effective normal stress, i.e., $\sigma^* = 0$. Shear stresses are shown by solid lines with colors representing different seamount height-to-width ratios. Dashed lines stand for yield strength ($=f_s\overline{\sigma}$), a proxy of effective normal stress on the seamount. The rupture propagates through the seamount for $h_s/w_b = 0.1$ (blue), but is stopped by the seamount for $h_s/w_b = 0.2$ (red) and 0.3 (green).

[9] We then explore how a seamount topographic anomaly ($h_s > 0$) affects σ^*_{min}. To approximate the seamount geometry, we use the two nodal points of the seamount base, up-dip at $d_s - w_b$ and down-dip at d_s, and a third point at the seamount top (h_s) to create a smooth spline curve employing the finite-element mesh generator, CUBIT. The spline curve represents the thrust interface at the location of the seamount. We keep other part of the megathrust fault identical to the planar fault model. An example of meshing with a seamount is shown in Figure S3. To explore the seamount parameter space listed in Table 2, we generate 112 mesh models in total. We then perform dynamic rupture simulations and search for σ^*_{min} for each model.

[10] Given the same seamount location and basal width, the amplitude of σ^*_{min} derived from a more realistic geometry mesh monotonically decreases as the seamount height-to-width ratio h_s/w_b increases (Figure 2). In other words, it is easier for a seamount to stop ruptures with a larger height-to-width ratio. As shown in Figure 3, a larger seamount height-to-width ratio h_s/w_b (i.e., a larger bending angle as rupture reaches the seamount) implies larger increase in normal stress and thus higher yield strength on the seamount, while the increase in shear stress is not sufficient to overcome the yield strength. For example, we consider a seamount of d^*=0.77, w^*=0.077, and σ^*=0, i.e., no perturbation to the effective normal stress on the seamount. The rupture propagates through the seamount with $h_s/w_b = 0.1$, in which the peak shear stress on the seamount is adequately large to overcome the yield strength when the rupture front arrived (blue curves in Figure 3). In comparison, ruptures are stopped by the seamount with $h_s/w_b = 0.2$ or larger (red and green curves in Figure 3), in which the peak shear stresses are below the yield strengths. Figure 3 clearly shows that an increased h_s/w_b sets a higher bar for the rupture to propagate through.

[11] The reduction in σ^*_{min} as a function of h_s/w_b also depends on d^* (Figure 2). If d^* is large, e.g., 0.92 (Figure 2d), the reduction in σ^*_{min} appears to be nearly a constant for all w^*. The effect of w^* on the σ^*_{min} reduction becomes more pronounced at smaller down-dip distance d^*. For instance, at d^*=0.46 (Figure 2a) and for a small seamount of w^*=0.077, σ^*_{min} is reduced by $\sim$20% when h_s/w_b is increased from 0 to 0.4. In contrast, σ^*_{min} only reduces by $\sim$5% for a larger seamount of w^*=0.308. Such dependence of the reduction rate of σ^*_{min} on d^* could be attributed to the different rupture propagation speed V_r/V_s as a rupture approaches the seamount. At large d^*, i.e., when the seamount is located at a short distance up-dip of the nucleation zone, the up-dip propagating rupture has not yet progressed to its full speed and hence is easier to be stopped (Figure 4). Therefore, the amplitude of σ^*_{min} is smaller for a larger d^*.

[12] Furthermore, we find that σ^*_{min} could be negative, suggesting that a subducted seamount of realistic geometry could stop coseismic ruptures even with a reduction in effective normal stress. Such cases would not be possible for a planar subduction megathrust model unless nonuniform frictional parameters or other fluid-induced mechanisms such as dilatancy strengthening are employed [*Yang et al.*, 2012; *Liu*, 2013; *Segall et al.*, 2010]. It has been proposed that seamount subduction may cause erosion of the overriding plate and thus result in the presence of fluids in the vicinity of the seamount [*Bangs et al.*, 2006]. The presence of entrained fluid-rich sediments could reduce effective normal stress and lubricate the fault [*Mochizuki et al.*, 2008]. Our results show that stopping ruptures is plausible even with a reduction in normal stress when taking into account of the realistic geometry of the seamount.

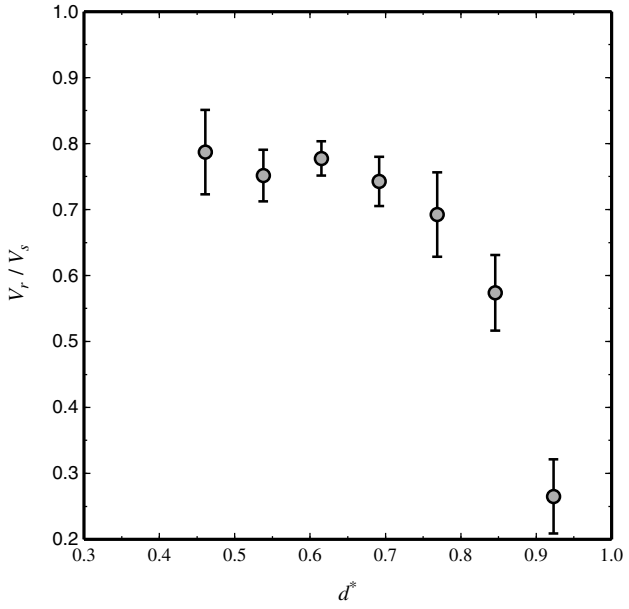

Figure 4. Change in the rupture speed V_r/V_s as a function of down-dip distance d^*. The rupture speed is computed at the down-dip edge of the seamount, where the rupture has not propagated into the seamount patch yet. Error bars indicate 95% confidence interval calculated for all simulation cases at the same d^*.

4. Discussion

[13] Our numerical experiments of dynamic ruptures are specifically designed to investigate the roles of realistic geometry of a subducted seamount in stopping ruptures. Therefore, we have ignored a few factors that may also influence rupture propagation. First, material contrast across the megathrust fault interface and off-fault damage may change the propagation speed of coseismic rupture and the rupture mode (crack versus pulse) [*Li et al*., 2007; *Yang and Zhu*, 2010; *Huang and Ampuero*, 2011; *Yang et al*., 2011]. Although the amplitude of $\sigma^*_{\min}$ might be different due to heterogeneous material properties, which are ignored in this study, the qualitative behaviors such as ruptures impeded by the seamount are similar. Second, we have assigned an artificially large value of fault strength at shallow depths to minimize the free surface effect. Previous numerical studies have shown that the free surface may strongly influence rupture propagation [*Kaneko and Lapusta*, 2010]. If a subducted seamount is close to the trench, then such free surface effect needs to be considered.

[14] Our model set up is similar to previous investigations of fault bending, branching, and off-fault failure induced by a dynamic rupture [*Duan and Oglesby*, 2005; *Rice et al*., 2005; *Bhat et al*., 2007], in which the rupture on the megathrust main fault is "branched" into slip along the curved top surface of the seamount. Our results have shown that d^* and h_s/w_b are critical parameters to determine the stress level for a seamount to stop ruptures. The rupture speed inversely correlates with d^* as a rupture approaches the seamount (Figure 4). Previous studies have suggested the rupture speed is an important factor to determine whether a dynamic rupture continues on the main fault or deviates to the branch. The h_s/w_b, approximately equivalent to a branching or bending angle, determines the changes in shear stress and yield strength on the fault (Figure 3). When h_s/w_b increases, the peak shear stress at the rupture front may not be sufficient to overcome the yield strength, thus a rupture may be stopped by the seamount (Figure 3). If a rupture is stopped by the seamount, both the shear stress and the yield strength on the seamount are increased (Figure 3). However, the difference between the yield strength and the shear stress is reduced to a value smaller than that before the rupture. Therefore, it would be easier to for the next rupture to propagate through, as observed from simulation results in multiple earthquake cycles [*Duan and Oglesby*, 2005; *Yang et al*., 2012]. Such process may also make the seamount a potential nucleation site for the next earthquake.

[15] *Wang and Bilek* [2011] have suggested that seamount subduction may generate a complex network of fractures in the overlying plate and that such a network of fractures and the associated heterogeneous stresses are unfavorable for the generation and propagation of large ruptures. Preliminary results of numerical modeling of seamount subduction with realistic geometry have shown that formation of large-scale thrust and normal faults in the overlying plate is plausible in the vicinity of the subducted seamount [*Ding and Lin*, 2012]. Although our results here cannot be used to directly evaluate the above fracture network model, we have quantitatively shown that coseismic ruptures can be stopped by a seamount even without a network of fractures in the overlying plate or elevation of effective normal stress near the seamount.

5. Conclusions

[16] We have performed slip-weakening dynamic rupture simulations considering seamount topographic features that are carried on the megathrust fault into subduction zones. For fixed depth and size of the earthquake rupture nucleation zone, our simulation results clearly show that a subducted seamount can act as a barrier, and such barrier effects are dependent on the seamount-to-nucleation distance and the seamount height-to-width ratio. The required additional effective normal stress to stop rupture is decreased as the seamount height-to-width ratio increases. This study demonstrates that when a seamount is subducted adjacent to the rupture nucleation zone, coseismic ruptures can be stopped even if the seamount has a lower effective normal stress than the ambient level. These dynamic modeling results indicate that subducted seamounts may stop earthquake ruptures for a wide range of seamount normal stress conditions, including the case of megathrust fault lubricated by seamount-top fluid-rich sediments. Our results suggest that realistic geometry of such topographic features needs to be considered when evaluating the roles of seamounts in affecting subduction zone earthquakes.

[17] **Acknowledgments.** We benefitted from discussions with Min Ding of the MIT/WHOI Joint Program. We thank two anonymous reviewers and the editor for valuable comments. This work was supported by NSF grant EAR-1015221 and WHOI Deep Ocean Exploration Institute awards 27071150 and 25051162. We are grateful to Brad Aagaard for his help on using the finite-element code, PyLith.

[18] The Editor thanks Benchun Duan and an anonymous reviewer for their assistance in evaluating this paper.

References

Aagaard, B., C. Williams, and M. Knepley (2008), PyLith: A finite-element code for modeling quasi-static and dynamic crustal deformation, *Eos Trans. AGU*, *89*(53), Fall. Meet. Suppl. Abstract T41A-1925.

Bangs, N. L. B., S. P. S. Gulick, and T. H. Shipley (2006), Seamount subduction erosion in the Nankai Trough and its potential impact on the seismogenic zone, *Geology*, *34*, 701–704, doi:10.1130/G22451.1.

Bhat, H. S., M. Olives, R. Dmowska, and J. R. Rice (2007), Role of fault branches in earthquake rupture dynamics, *J. Geophys. Res.*, *112*, B11309, doi:10.1029/2007JB005027.

Cloos, M. (1992), Thrust-type subduction-zone earthquakes and seamount asperities: A physical model for seismic rupture, *Geology*, *7*, 601–604, doi:10.1130/0091-7613.

Day, S. M., L. A. Dalguer, and N. Lapusta (2005), Comparison of finite difference and boundary integral solutions to three-dimensional spontaneous rupture, *J. Geophys. Res.*, *110*, B12307, doi:10.1029/2005JB003813.

Ding, M., and J. Lin (2012), Effects of a subducting seamount on the overriding plate deformation and faulting, *Eos Trans. AGU*, *91*(52), Fall Meet. Suppl. Abstract, T11A-2530.

Duan, B. (2012), Dynamic rupture of the 2011 Mw 9.0 Tohoku-Oki earthquake: Roles of a possible subducting seamount, *J. Geophys. Res.*, *117*, B05311, doi:10.1029/2011JB009124.

Duan, B., and D. D. Oglesby (2005), Multicycle dynamics of nonplanar strike-slip faults, *J. Geophys. Res.*, *110*, B03304, doi:10.1029/2004JB003298.

Harris, R. A., et al. (2009), The SCEC/USGS dynamic earthquake rupture code verification exercise, *Seismol. Res. Lett.*, *80*, 119–126, doi:10.1785/gssrl.80.1.119.

Hicks, S. P., A. Rietbrock, C. A. Haberland, I. M. A. Ryder, M. Simons, and A. Tassara (2012), The 2010 Mw 8.8 Maule, Chile earthquake: Nucleation and rupture propagation controlled by a subducted topographic high, *Geophys. Res. Lett.*, *39*, L19308, doi:10.1029/2012GL053184.

Huang, Y., and J. P. Ampuero (2011), Pulse-like ruptures induced by low-velocity fault zones, *J. Geophys. Res.*, *116*, B12307, doi:10.1029/2011JB008684.

Husen, S., E. Kissling, and R. Quintero (2002), Tomographic evidence for a subducted seamount beneath the Gulf of Nicoya, Costa Rica: the cause of the 1990 Mw = 7.0 Gulf of Nicoya earthquake, *Geophys. Res. Lett.*, *29*(8), 1238, doi:10.1029/2001GL014045.

Ida, Y. (1972), Cohesive force across the tip of a longtitudinal-shear crack and Griffith's specific surface energy, *J. Geophys. Res.*, *77*, 3796–3805.

Kaneko, Y., and N. Lapusta (2010), Supershear transition due to a free surface in 3-D simulations of spontaneous dynamic rupture on vertical strike-slip faults, *Tectonophysics*, *493*, 272–284, doi:10.1016/j.tecto.2010.06.015.

Kodaira, S., N. Takahashi, A. Nakanishi, S. Miura, and Y. Kaneda (2000), Subducted seamount imaged in the rupture zone of the 1946 Nankaido earthquake, *Science*, *289*, 104–106.

Li, H., L. Zhu, and H. Yang (2007), High-resolution structures of the Landers fault zone inferred from aftershock waveform data, *Geophys. J. Int.*, *171*, 1295–1307, doi:10.1111/j.1365246X.2007.03608.x.

Liu, Y. (2013), Numerical simulations on megathrust rupture stabilized under strong dilatancy strengthening in slow slip region, *Geophys. Res. Lett.*, *40*, 1311–1316, doi:10.1002/grl.50298.

Mochizuki, K., T. Yamada, M. Shinohara, Y. Yamanaka, and T. Kanazawa (2008), Weak inter-plate coupling by seamounts and repeating M∼7 earthquakes, *Science*, *321*, 1194–1197.

Noda, H., and N. Lapusta (2010), Three-dimensional earthquake sequence simulations with evolving temperature and pore pressure due to shear heating: Effect of heterogeneous hydraulic diffusivity, *J. Geophys. Res.*, *115*, B12314, doi:10.1029/2010JB007780.

Rice, J. R. (1992), Fault stress states, pore pressure distributions, and the weakness of the San Andreas Fault, in *Fault Mechanics and Transport Properties in Rocks*, edited by B. Evans and T.-F. Wong, pp. 475–503, Elsevier, New York.

Rice, J. R., C. G. Sammis, and R. Parsons (2005), Off-fault secondary failure induced by a dynamic slip pulse, *Bull. Seismol. Soc. Am.*, *95*, 109–134, doi:10.1785/0120030166.

Saffer, D. M., and H. J. Tobin (2011), Hydrogeology and mechanics of subduction zone fore-arcs: Fluid flow and pore pressure, *Annu. Rev. Earth Planet. Sci.*, *39*, 157–186, doi:10.1146/annurev-earth-040610-133408.

Scholz, C. H., and C. Small (1997), The effect of seamount subduction on seismic coupling, *Geology*, *25*, 487–490.

Segall, P., A. M. R. A. M. Bradley, and J. R. Rice (2010), Dilatant strengthening as a mechanism for slow slip events, *J. Geophys. Res.*, *115*, B12305, doi:10.1029/2010JB007449.

Simons, M., et al. (2011), The 2011 Magnitude 9.0 Tohoku-Oki earthquake: Mosaicking the megathrust from seconds to centuries, *Science*, *332*, 1421–1427, doi:10.1126/science.1206731.

Singh, S. C., et al. (2011), Aseismic zone and earthquake segmentation associated with a deep subducted seamount in Sumatra, *Nat. Geosci.*, *4*, 308–311, doi:10.1038/NGEO1119.

Trehu, A. M., R. J. Blakely, and M. C. Williams (2012), Subducted seamounts and recent earthquakes beneath the central Cascadia forearc, *Geology*, *40*, 103–106, doi:10.1130/G32460.1.

Uenishi, K., and J. R. Rice (2003), Universal nucleation length for slip-weakening rupture instability under nonuniform fault loading, *J. Geophys. Res.*, *108*(B1), 2042, doi:10.1029/2001JB001681.

Wang, K., and S. L. Bilek (2011), Do subducting seamounts generate or stop large earthquakes?, *Geology*, *39*, 819–822, doi:10.1130/G31856.1.

Yang, H., and L. Zhu (2010), Shallow low-velocity zone of the San Jacinto fault from local earthquake waveform modelling, *Geophys. J. Int.*, *183*, 421–432, doi:10.1111/j.1365246X.2010.04744.x.

Yang, H., L. Zhu, and E. S. Cochran (2011), Seismic structures of the Calico fault zone inferred from local earthquake travel time modelling, *Geophys. J. Int.*, *186*, 760–770, doi:10.1111/j.1365-246X.2011.05055.x.

Yang, H., Y. Liu, and J. Lin (2012), Effects of subducted seamounts on megathrust earthquake nucleation and rupture propagation, *Geophys. Res. Lett.*, *39*, L24302, doi:10.1029/2012GL053892.